

# Atomic-scale analysis of carbon partitioning between martensite and austenite by atom probe tomography and correlative transmission electron microscopy

Yuki Toji<sup>a,b,\*</sup>, Hiroshi Matsuda<sup>b</sup>, Michael Herbig<sup>a</sup>, Pyuck-Pa Choi<sup>a</sup>, Dierk Raabe<sup>a</sup>

<sup>a</sup> Max-Planck-Institut für Eisenforschung GmbH, Max-Planck-Str. 1, 40237 Düsseldorf, Germany

<sup>b</sup> Steel Research Laboratory, JFE Steel Corporation, 1 Kawasaki-cho, Chuo-ku, Chiba 260-0835, Japan

Received 24 April 2013; received in revised form 22 October 2013; accepted 28 October 2013

Available online 23 November 2013

## Abstract

Carbon partitioning between ferritic and austenitic phases is essential for austenite stabilization in the most advanced steels such as those produced by the quenching and partitioning (Q&P) process. The atomistic analysis of the carbon partitioning in Q&P alloys is, however, difficult owing to the simultaneous occurrence of bainite transformation, which can also contribute to carbon enrichment into remaining austenite and hence overlap with the carbon partitioning from martensite into austenite. Therefore, we provide here a direct atomic-scale evidence of carbon partitioning from martensite into austenite without the presence of bainite transformation. Carbon partitioning is investigated by means of atom probe tomography and correlative transmission electron microscopy. A model steel (Fe–0.59 wt.% C (2.7 at.% C)–2.0 wt.% Si–2.9 wt.% Mn) with martensite finish temperature below room temperature was designed and used in order to clearly separate the carbon partitioning between martensite and austenite from the bainite transformation. The steel was austenitized at 900 °C, then water-quenched and tempered at 400 °C. Approximately 8 vol.% retained austenite existed in the as-quenched state. We confirmed by X-ray diffraction and dilatometry that austenite decomposition via bainite transformation did not occur during tempering. No carbon enrichment in austenite was observed in the as-quenched specimen. On the other hand, clear carbon enrichment in austenite was observed in the 400 °C tempered specimens with a carbon concentration inside the austenite of 5–8 at.%. The results hence quantitatively revealed carbon partitioning from martensite to austenite, excluding bainite transformation during the Q&P heat treatment.

© 2013 Acta Materialia Inc. Published by Elsevier Ltd. All rights reserved.

**Keywords:** Quenching and partitioning; Martensite; Austenite; Bainite; Atom probe tomography

## 1. Introduction

Fundamental research on advanced steels is confronted with an increasing demand for realizing high-strength alloys that enable the design of highly fuel-efficient vehicles with maximum passive passenger safety [1,2]. One essential high-strength steel for applications in car bodies is the transformation-induced plasticity (TRIP) grade [3]. These steels contain retained austenite and hence show excellent

ductility. However, the tensile strengths of conventional low-carbon TRIP steels with microstructures consisting of ferrite, carbide-free bainite, retained austenite and small amounts of martensite generally do not exceed 1100 MPa [3–6]. This limitation is due to the fact that their ferrite volume fraction is normally too high so as to accumulate a sufficient amount of carbon into austenite during intercritical annealing and following austempering to obtain stable retained austenite. In order to achieve a higher strength level above 1100 MPa while maintaining high ductility, several novel steels that utilize retained austenite have been developed in the last decade, such as nanocrystalline

\* Corresponding author at: Max-Planck-Institut für Eisenforschung GmbH, Max-Planck-Str. 1, 40237 Düsseldorf, Germany.

E-mail address: [y-toji@jfe-steel.co.jp](mailto:y-toji@jfe-steel.co.jp) (Y. Toji).

bainitic steel (or super bainite) [7,8], maraging-TRIP steel [6,9,10] and quenching and partitioning (Q&P) steel [11,12].

Q&P steels yield an excellent balance of high tensile strength and good elongation with similar chemical compositions as conventional TRIP steels [12]. They are produced via the Q&P process which consists of a quenching and a partitioning step. In the quenching step, fully austenitized or intercritically annealed steels are quenched to temperatures (hereafter referred to as the “quench temperature”) below the martensite start ( $M_s$ ) temperature but above the martensite finish ( $M_f$ ) temperature in order to form a controlled volume fraction of martensite. The quenched steels are then held at the same or higher temperatures than the quench temperature during the subsequent partitioning step. Austenite that prevails after quenching is considered to be stabilized through carbon partitioning from martensite into the austenite during the partitioning treatment. The resultant microstructures of the steels mainly consist of tempered martensite and retained austenite so that a higher strength can be achieved as compared to conventional TRIP steels.

Carbon partitioning between ferritic and austenitic phases is essential for all austenite stabilization phenomena in most advanced steels such as those encountered in the Q&P process. The atomistic analysis of carbon partitioning in Q&P alloys is, however, challenging owing to the overlap of several competing phenomena during the partitioning step. It has been suggested that the carbon partitioning from martensite into austenite is controlled by the constrained carbon equilibrium (CCE) criterion [11]. This criterion aims at predicting the carbon concentration in austenite under the condition that (1) an identical carbon chemical potential exists in both ferrite (or martensite) and austenite; and that (2) the atomic balancing proceeds under the assumption that the interface between ferrite and austenite does not migrate. Therefore, this model does not account for the volume expansion frequently observed during the partitioning step [13–17]. Possible reasons, as mentioned by Santofimia et al. [16], to explain the volume expansion are the bainite transformation [15–18] or the migration of martensite/austenite interface [14–16,19,20], in cases where the partitioning temperature is above the  $M_s$  temperature. The bainite transformation can also contribute to carbon enrichment into the remaining austenite if carbide precipitation is suppressed, for example, through the addition of Si [21]. The migration of the martensite/austenite interface should also have some influence on carbon enrichment into austenite [20]. Therefore, it is essential to separate the contributions to the carbon enrichment into austenite during the Q&P heat treatment caused by the carbon partitioning from martensite (addressed in this work) from that caused by the other possible mechanisms mentioned above (excluded from this work). Such knowledge is not only important for the further understanding of the Q&P process but also for the more precise prediction of microstructures and

resultant mechanical properties of other advanced high-strength steels.

The Q&P process has mainly been applied to steels with chemical compositions similar to those of conventional TRIP steels [12,15]. In such steels, bainite formation is practically unavoidable [15] as the chemical compositions are designed to promote bainite formation during austempering in the same temperature range as the partitioning step. This makes it difficult to distinguish the contributions to carbon enrichment into austenite during the partitioning step caused by the bainite transformation from that caused by the carbon partitioning from martensite. Recently, Santofimia et al. [16] tried in an elegant study to address this point by separating the contributions of these two phenomena using a high Ni and Cr containing steel to avoid bainite transformation. The data, however, seem to indicate that the face-centered cubic (fcc) to body-centered cubic (bcc) transformation could not be entirely suppressed during partitioning as a slight volume expansion of the specimens was observed. Bigg et al. [22] reported on carbon enrichment into austenite without the occurrence of bainite transformation by means of in situ neutron measurement during reheating an as-quenched martensite containing ~30 vol.% austenite. However, up to now there is no direct atomic-scale evidence of carbon partitioning from martensite into austenite without the interference of bainite.

Therefore, this study aims at providing direct atomic scale evidence of carbon partitioning from martensite into austenite during a Q&P heat treatment excluding the bainite transformation. Carbon partitioning is investigated in detail by means of atom probe tomography (APT) [23–32] and correlative transmission electron microscopy (TEM), conducted directly on APT samples.

## 2. Experimental procedure

### 2.1. Model alloy design and processing

For separating carbon partitioning between martensite and austenite from bainite transformation and/or interface migration, a chemical composition with  $M_s$  and  $M_f$  temperatures, respectively, above and below room temperature was selected. Fig. 1 shows the comparison between (a) the heat treatment applied in this study and (b) a general Q&P heat treatment. The bottom figures schematically show the relationship between partitioning time and retained austenite ( $\gamma$ ) volume fraction as measured by, for instance, X-ray diffraction (XRD) at room temperature after cooling from the partitioning temperature (PT). In the case of the general Q&P heat treatment (Fig. 1b), the remaining austenite at the quench temperature (QT) is unstable at room temperature so that the retained austenite volume fraction before partitioning treatment, which is measured at room temperature, is almost zero. Therefore, the exact amount of austenite remaining at the quench temperature can generally not be measured and hence has to be estimated, for instance, by using the Koistinen–Marburger

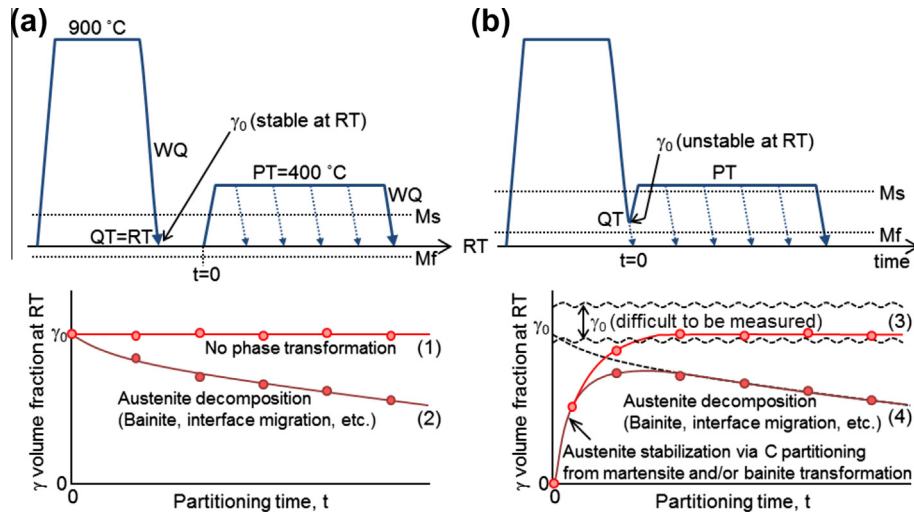


Fig. 1. Comparison between (a) the heat treatment applied in this study and (b) a general Q&P heat treatment. The bottom figures schematically show the relationship between partitioning time and retained austenite ( $\gamma$ ) volume fraction as measured by, for instance, XRD at room temperature after cooling from PT. RT: room temperature, QT: quench temperature, PT: partitioning temperature,  $M_s$ : martensite start temperature,  $M_f$ : martensite finish temperature, WQ: water-quenching,  $\gamma_0$ : austenite volume fraction at QT. Dotted wavy lines in (b) express the uncertainty of the initial austenite volume fraction,  $\gamma_0$ .

equation [33]. The remaining austenite at the quench temperature is stabilized through the carbon partitioning from martensite and/or the bainite transformation. The austenite volume fraction measured at room temperature increases with the stabilization process, regardless of whether austenite decomposition occurs (indicated by case 4 in the figure) or not (indicated by case 3 in the figure). Even if the volume fraction becomes stable for longer partitioning times such as indicated by case 3, the value cannot be compared with the exact initial austenite fraction ( $\gamma_0$ ) due to the reason mentioned above. Therefore, the austenite volume fraction measured at room temperature does typically not enable one to decide whether austenite decomposition occurs or not during the partitioning treatment. In contrast, in the heat treatment applied in this study (Fig. 1a), the remaining austenite after the first quenching is stable at room temperature (without the partitioning step) and hence its volume fraction can be quantified. It should be noted that the stability of the remaining austenite should not decline during the partitioning step since its carbon concentration does not decrease during the partitioning step unless carbide precipitation occurs in austenite, which can be suppressed by Si [21]. If austenite decomposition occurs during the partitioning step, the volume fraction of austenite must decrease. Therefore, it can be concluded from the austenite volume fraction change measured at room temperature whether austenite decomposition occurs (indicated by case 2) or not (indicated by case 1), during the partitioning process.

The actual chemical composition was Fe–0.59 wt.% C (2.7 at.% C)–2.0 wt.% Si–2.9 wt.% Mn–0.038 wt.% Al. The carbon content in this model alloy was higher than that in typical alloys to which Q&P processes have been applied

[12,15] in order to lower the  $M_f$  temperature below room temperature. The high amount of Si (2 wt.%) was added to suppress carbide formation [21]. The steel was prepared by vacuum induction melting. The ingot was homogenized at 1240 °C for 48 h, then air-cooled to room temperature. The homogenized ingot was reheated and held at 1200 °C for 30 min followed by hot rolling to a sheet with a thickness of 3.6 mm, then air-cooled to room temperature. Specimens with dimensions of 15 mm  $\times$  50 mm, cut from the hot-rolled steel sheet, were then heat-treated according to Fig. 1a. They were austenitized at 900 °C for 3 min, then water-quenched, followed by a partitioning step (which is the same as the tempering process of martensite in this case) at 400 °C for 10–3000 s in a salt bath furnace. The specimens before and after tempering are hereafter referred to as “as-quenched specimen” and “tempered specimen”, respectively. Although slight decarburization occurred near the surface during homogenization and reheating, it was confirmed that the carbon concentration at least at one quarter of the thickness of the hot band was identical with the bulk carbon concentration. Therefore, all following characterization was performed at one quarter of the thickness of the hot band to avoid the decarburized layer.

## 2.2. Microstructure characterization

The amount of retained austenite was quantified by XRD with  $\text{Co } K_\alpha$  radiation from the intensities of the (110) $\alpha$ , (200) $\alpha$ , (211) $\alpha$ , (220) $\alpha$ , (111) $\gamma$ , (200) $\gamma$ , (220) $\gamma$ , (311) $\gamma$  and (222) $\gamma$  reflections. The carbon concentration in retained austenite was calculated from the lattice parameter  $a_\gamma$  (Å) obtained from the  $\gamma$  reflections using the following equation [34], which is a combination of the equations of Ruhl et al. [35] for C, Mn and Si and Dyson et al. [36] for Al:

$$a_{\gamma} (\text{\AA}) = 3.572 + 0.033[\text{C}] + 0.0012[\text{Mn}] - 0.00157[\text{Si}] + 0.0056[\text{Al}] \quad (1)$$

where [C], [Mn], [Si] and [Al] are the concentrations of carbon, manganese, silicon and aluminum in austenite (in wt.%), respectively. The samples for XRD were ground from the surface to one-quarter of the thickness of the heat-treated steels, and subsequently another 100  $\mu\text{m}$  was removed from the ground surface using a mixture of oxalic acid and hydrogen peroxide to exclude the influence of strain introduced by the grinding.

Dilatation was probed using a Bähr Dil805 to measure the  $M_s$  temperature and to investigate the volume change during tempering after water-quenching. The samples for the dilatation measurement were taken from one-quarter of the thickness of the hot-rolled or the water-quenched steels with dimensions of 4 mm  $\times$  9 mm  $\times$  1 mm. To measure the  $M_s$  temperature, the sample was heated and held at 900  $^{\circ}\text{C}$  for 3 min followed by rapid cooling using hydrogen gas to room temperature. The cooling rate from 900  $^{\circ}\text{C}$  to 100  $^{\circ}\text{C}$  was  $\sim 200$   $^{\circ}\text{C s}^{-1}$ . The measured  $M_s$  temperature of this steel was 205  $^{\circ}\text{C}$ .

Microstructures in the cross-section perpendicular to the transverse direction (TD cross-section) etched with 0.1% Nital were observed by scanning electron microscopy (SEM). Electron backscatter diffraction (EBSD) measurements were performed with a step size of 50 nm to distinguish austenite from martensite.

### 2.3. Atomic scale analysis by APT

APT [23–32] was applied for the near-atomic quantitative investigation of carbon partitioning during tempering. Samples for APT measurements were prepared using focused ion beam (FIB) milling and the lift-out procedure described in Ref. [37]. APT analyses were performed using a local electrode atom probe (LEAP 3000X HR, Cameca Instruments) in voltage mode at a specimen temperature of  $\sim 65$  K. The pulse fraction and the pulse rate were 15% and 200 kHz, respectively. Data analyses were performed using the IVAS software (Cameca Instruments). The acquired mass spectra revealed peaks corresponding to  $\text{C}^+$ ,  $\text{C}_2^+$ ,  $\text{C}_3^+$ ,  $\text{C}_3^{2+}$ ,  $\text{C}_4^+$ ,  $\text{C}_4^{2+}$ ,  $\text{Fe}^{2+}$ ,  $\text{Si}^{2+}$ ,  $\text{Mn}^{2+}$ ,  $\text{Al}^{2+}$  and  $\text{Al}^{3+}$ . In most analyses, the  $(^{12}\text{C}_3^{13}\text{C})^{2+}$  peak at a mass-to-charge ratio (Da) of 24.5 was detected. This means that the peak at 24 Da, 25 Da and 26 Da could be due to either  $\text{C}_2^+$  or  $\text{C}_4^+$ , or a mixture of both [38,39]. Therefore, a peak decomposition algorithm supplied by the IVAS software was applied to decompose these peaks. Although the 27 Da peak could also be decomposed into  $\text{Al}^+$  and  $^{54}\text{Fe}^{2+}$  [40], the contribution of  $\text{Al}^+$  to the 27 Da peak was not taken into account. Therefore, the Fe concentration analyzed by APT might be slightly overestimated, even though the contribution of  $\text{Al}^+$  as compared with that of  $^{54}\text{Fe}^{2+}$  to the 27 Da peak should be small according to the low nominal Al content (0.038 wt.%) of the alloy.

Although APT is a powerful method for investigating the position of light atoms such as carbon at the near-atomic scale, the characterization of phase transformation and partitioning by APT alone is often insufficient. The spatial resolution of APT depends on the material and measurement conditions and is as a rule not sufficient for the reconstruction of crystal lattices. In addition, in the present case, martensite transformation of retained austenite can occur at the cryogenic temperature inside the atom probe chamber (around 65 K in the present case). This means that even though a grain region could be correctly identified as martensite from its lattice parameter in the atom probe data set, it might have been austenite before the APT measurement. In order to provide direct evidence that certain regions in the APT data are indeed austenite, phase identification was performed by scanning nano-beam diffraction (spot size: 0.5 nm, step size: 2 nm, exposure time: 20 ms) using the commercial setup ASTAR [41,42] by Nanomegas prior to the APT measurement in a JEOL JEM 2200FS transmission electron microscope operated at 200 kV, directly on the as-prepared APT samples using a dedicated setup [43].

## 3. Results

### 3.1. Confirmation of the absence of bainite transformation during the partitioning step

Fig. 2a shows the austenite volume fraction of the as-quenched and tempered specimens measured by XRD at room temperature. Approximately 8 vol.% of austenite exists in the as-quenched specimen, which means that the  $M_f$  temperature of the steel is indeed below room temperature. The austenite volume fraction in the specimens does not change by tempering up to 3000 s. This indicates that austenite decomposition, i.e. bainite transformation, did not occur under the tempering conditions in this study. Fig. 2b and c presents the austenite lattice parameter of the same specimens shown in Fig. 2a, measured by XRD, and the carbon concentration in austenite (in at.%) as calculated from the lattice parameter using Eq. (1), respectively. The austenite lattice parameter increases with tempering time, and the carbon concentration in the austenite increases corresponding to the increase in the lattice parameter, even though the austenite carbon concentration of the as-quenched specimen was calculated to be below zero, which will be discussed later. Fig. 3 shows the dilatation curve during tempering at 400  $^{\circ}\text{C}$  of the as-quenched specimen. No volume expansion, which would indicate bainite transformation [15–17], was observed. Instead, a slight contraction occurred, which could be caused by carbide precipitation [44]. From the results of both XRD and dilatation measurements, we conclude that no bainite transformation occurred under the current experimental conditions. Hence, only the contribution of carbon partitioning from martensite to austenite, completely excluding

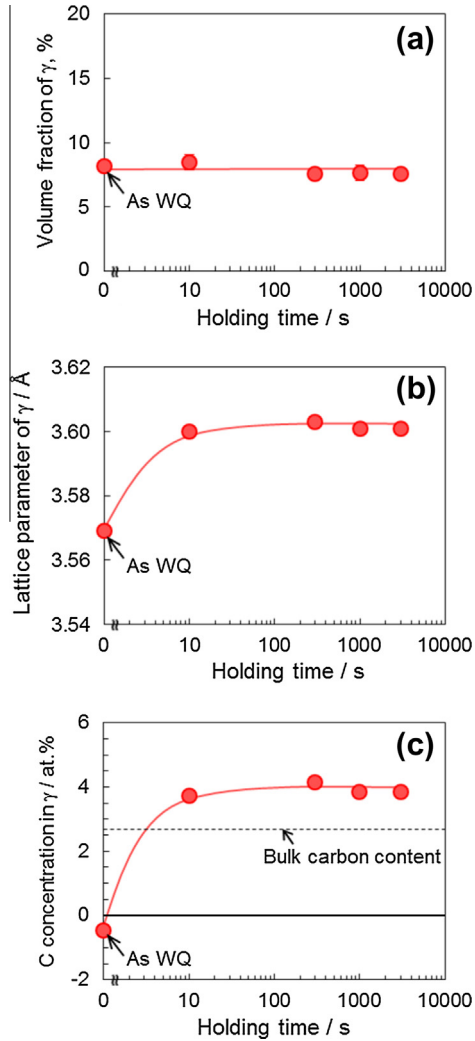


Fig. 2. Change in austenite volume fraction (a), austenite lattice parameter (b) and carbon concentration in austenite (c) during tempering at 400 °C obtained by XRD.  $\gamma$ : austenite, WQ: water-quenching. The error bars in (a) represent the one-sigma statistical error.

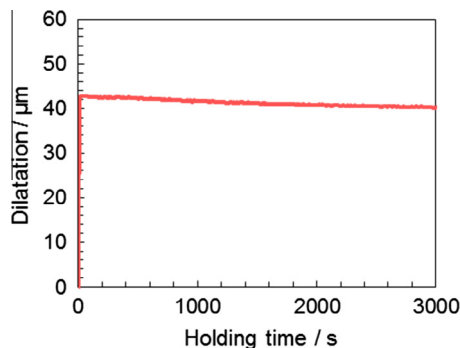


Fig. 3. Dilatation curve during tempering at 400 °C of as-quenched specimen.

the influence of bainite transformation, is considered in the rest of this paper. The as-quenched specimen and the 400 °C tempered specimens for 10 s and 300 s will be discussed in detail in the following.

### 3.2. SEM microstructure

Fig. 4 shows SEM microstructures of the as-quenched specimen and specimens tempered at 400 °C for 10 s and 300 s, respectively. No remarkable contrast can be seen in the as-quenched specimen. In the tempered specimens, many plate-shaped precipitates with white contrast are observed, which are considered to be carbides. From the comparison between the SEM image and the phase map obtained by EBSD (Fig. 5a and b), the relatively large flat grains with white contrast in the SEM image can be recognized as retained austenite. The retained austenite appears to exist on prior austenite grain boundaries, packet boundaries and block boundaries (Fig. 5c). Although thin film-like austenite layers between martensite laths are also expected [45–47], they are barely visible due to the limited resolution of EBSD.

### 3.3. Identification of phases by correlative TEM and APT

Before investigating carbon partitioning during tempering by APT, an example is presented which provides direct evidence that certain regions in APT data are indeed austenite. Crystallographic structures of phases existing inside APT samples were confirmed by conducting TEM observation directly on the APT samples prior to the APT measurement [43]. Fig. 6a shows an example of a TEM image of an APT sample taken from the specimen tempered at 400 °C for 300 s. The tip of the sample was clearly identified as austenite by TEM diffraction patterns (Fig. 6b). Fig. 6c shows the C atom map of the same sample obtained by APT from the same perspective as the TEM image (Fig. 6a), while Fig. 6d shows the C atom map from another perspective rotated by 90° relative to Fig. 6c. The yellow envelopes in the map indicate the iso-concentration surfaces representing 2.7 at.% C (same as the bulk concentration). There is a clear interface between carbon-enriched and carbon-depleted regions. From comparison of the TEM image shown in Fig. 6a, the phase map (Fig. 6b) and the C atom maps (Fig. 6c and d), it is obvious that the carbon-enriched region is austenite. The carbon concentration inside the marked cylinder in the austenite region was analyzed as 5.61 at.%, which is much higher than the bulk concentration (2.7 at.%) but substantially lower than the carbon concentration in cementite (25 at.%) or  $\epsilon$ -carbide (25–33 at.%). Therefore, the regions which contain ~6 at.% C are regarded as austenite in the following discussion.

### 3.4. Change in the carbon distribution during tempering

Fig. 7 shows atom maps of C, Fe, Mn and Si of the as-quenched specimen and concentration profiles along the black arrow indicated in the C atom map. Although the substitutional elements (Fe, Mn, Si) are distributed uniformly, the carbon concentration fluctuates in the range between 1.5 at.% and 4.5 at.% in the as-quenched state.

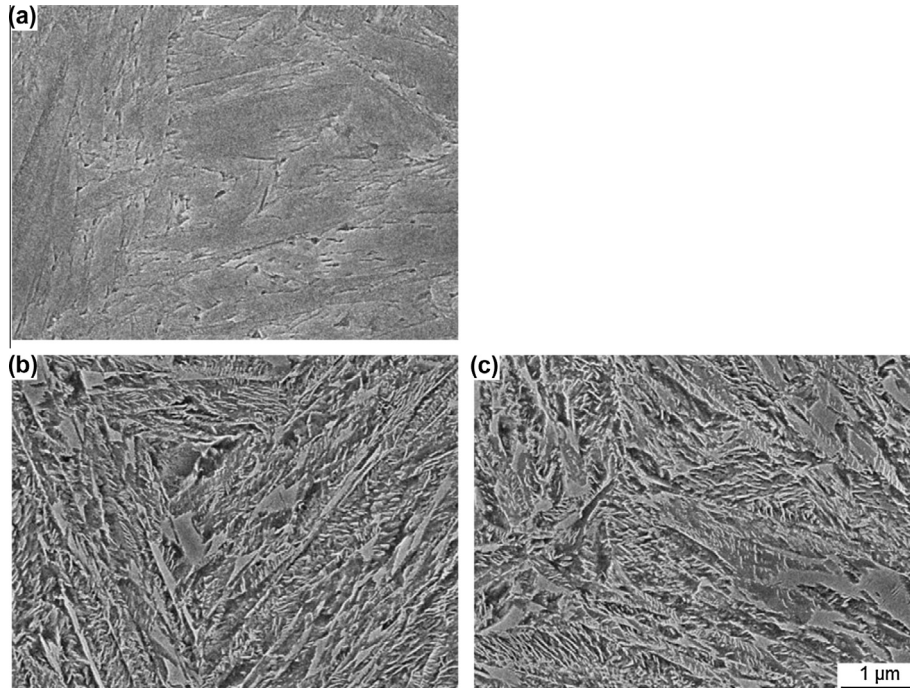


Fig. 4. SEM microstructures of the specimens (a) as-quenched, (b) tempered at 400 °C for 10 s and (c) tempered at 400 °C for 300 s.

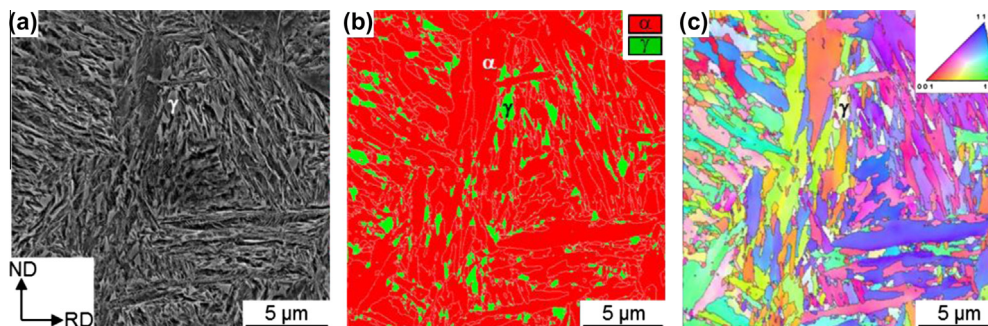


Fig. 5. Comparison between SEM image (a), phase map (b) and inverse pole figure map (c) obtained by EBSD of the specimen tempered at 400 °C for 300 s. White lines in (b) and black lines in (c) represent high-angle boundaries (15–180°).  $\alpha$ : martensite,  $\gamma$ : austenite, ND: normal direction, RD: rolling direction. (For interpretation of the references to color in this figure legend, the reader is referred to the web version of this article.)

However, no regions that are regarded as austenite were found in any of the eight APT samples taken from the as-quenched specimen, which were seen in the tempered specimens shown later. This means that the carbon partitioning from martensite to austenite during water-quenching and sample storage at room temperature was essentially negligible, which will be discussed later. The average carbon concentration in these eight as-quenched samples analyzed by APT was 2.77 at.%. This value is in good agreement with the bulk carbon content of the steel (2.7 at.%).

During tempering, carbon redistribution occurred rapidly. Fig. 8 shows atom maps of C, Fe, Mn and Si of the specimen tempered at 400 °C for 10 s, and concentration profiles along the arrow indicated in the C atom map. The yellow envelopes in the C atom map are the isoconcentration surfaces representing 2.7 at.% carbon. After

tempering for only 10 s, carbon partitioning is clearly seen as compared with the as-quenched specimen (Fig. 7a). There are several carbon-enriched regions in the lower part of the C atom map. These regions cannot be unambiguously identified, but they could be carbon segregation to dislocations or boundaries, carbon clusters or carbides, according to their rod or thin-plate shape. On the other hand, the carbon-enriched region in the upper part of the C atom map is larger than the other carbon-enriched features mentioned above. The carbon concentration in this region is  $\sim 6$  at.% (Fig. 8b), which is similar to the carbon concentration in austenite as shown in Fig. 6. Therefore, this region is identified as austenite. Substitutional elements are still distributed uniformly, indicating that only carbon partitioning occurred during tempering at 400 °C for 10 s.

Fig. 9a shows atom maps of C, Fe, Mn and Si of the specimen tempered at 400 °C for 300 s, where

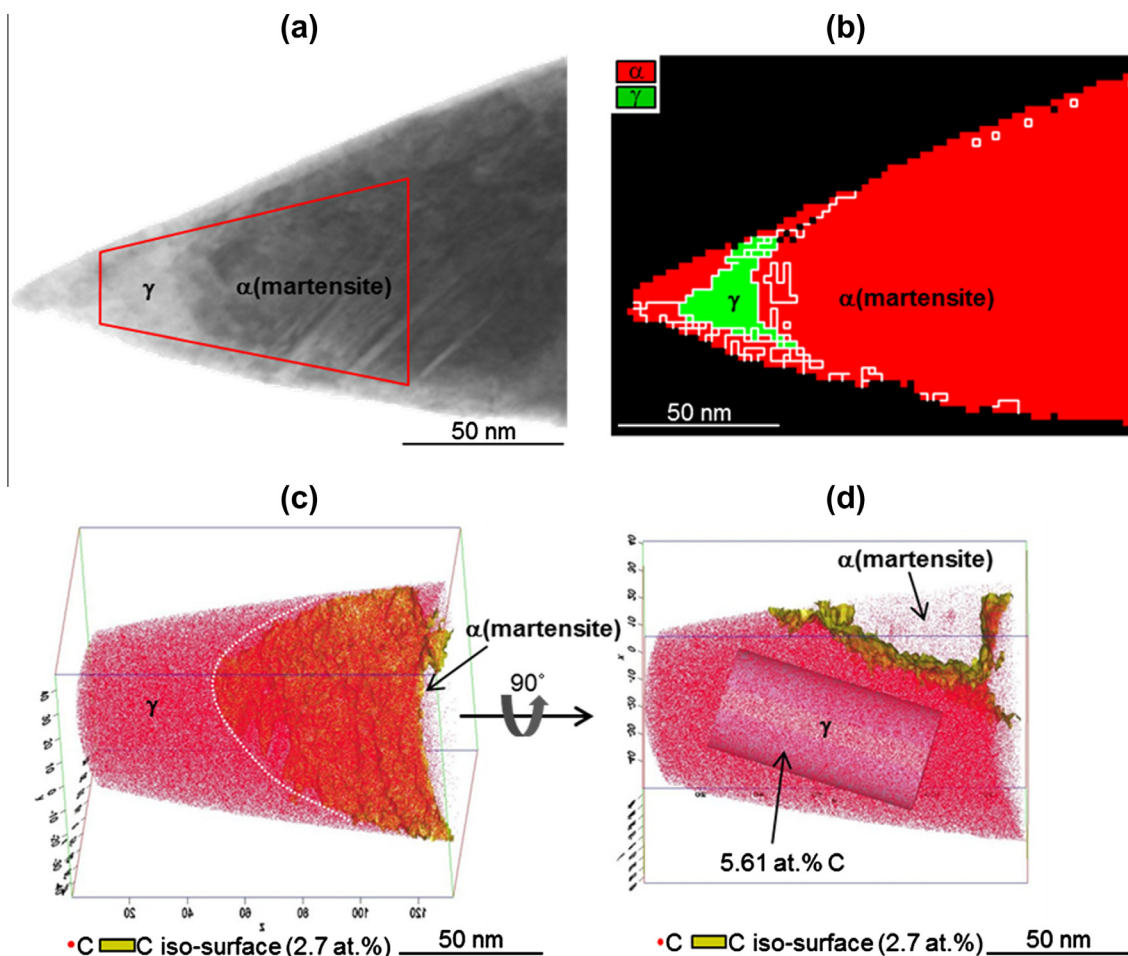


Fig. 6. Comparison between (a) TEM image, (b) phase map obtained by diffraction patterns in TEM on the APT sample and (c and d) C atom maps obtained by APT of the specimen tempered at 400 °C for 300 s. The yellow surfaces in (c) and (d) are the isoconcentration surfaces with 2.7 at.% C.  $\alpha$ : martensite,  $\gamma$ : austenite. (For interpretation of the references to color in this figure legend, the reader is referred to the web version of this article.)

isoconcentration surfaces representing 2.7 at.% C are displayed in yellow. Plate-shaped carbon-enriched objects with  $\sim 5$  nm thickness are clearly observed. Fig. 9b and c shows the averaged compositions of C, Fe, Mn, Si relative to the position of the interface around the carbon-enriched object, which is indicated by the arrow in the bottom part of the C atom map (Fig. 9a). Such an analysis is referred to as a proximity histogram (proxigram) [48]. The interface was here defined as the plane that marks the median of the carbon concentration gradient around the interface, 10 at.% C in the present case. Regarding Fe, Mn and Si, the substitutional atomic fractions, i.e. the number of each atom divided by the total number of substitutional atoms (Fe, Mn, Si and Al), are shown. The carbon concentration inside the object indicated by the arrow in Fig. 9a is almost 25 at.%, which is the stoichiometric carbon concentration in cementite. However, it is not entirely clear whether this object is indeed cementite or other transition carbide. Therefore, such types of carbon-enriched regions are hereafter referred to as “carbide”. The substitutional atomic fraction of Fe is identical both inside and outside the carbide, whereas that of Si is slightly lower and that of Mn is slightly higher inside the carbide. Miyamoto et al.

reported that Si and Mn did not partition between  $\varepsilon$ -carbide and ferrite matrix, whereas Si partitioned between cementite and ferrite [49]. The partitioning of Si and Mn between carbide and ferrite observed in this study is not so clear as that reported in Ref. [49]. However, the observed slight partitioning may indicate that the carbide is in a state of transition from metastable carbide such as  $\varepsilon$ -carbide to stoichiometric cementite. In the Fe, Mn and Si atom maps (Fig. 9a), enrichment of these atoms inside the carbide is also observed. However, as shown in Fig. 9c, the Fe atomic fraction was identical both inside and outside the carbide, and the atomic density inside the carbide was confirmed to be higher than that outside the carbide. Therefore, this observation is attributed to an artifact known as the local magnification effect [50]. As the carbide has a lower evaporation field than the surrounding matrix, the detected number of atoms inside the carbide is higher. Although this artifact affects the position and/or width of the interface, it does not significantly affect the elemental concentration inside the particle.

Fig. 10 shows another feature detected in the specimen tempered at 400 °C for 300 s. Fig. 10b shows atom maps of C, Fe, Mn and Si inside the cylinder shown in the C

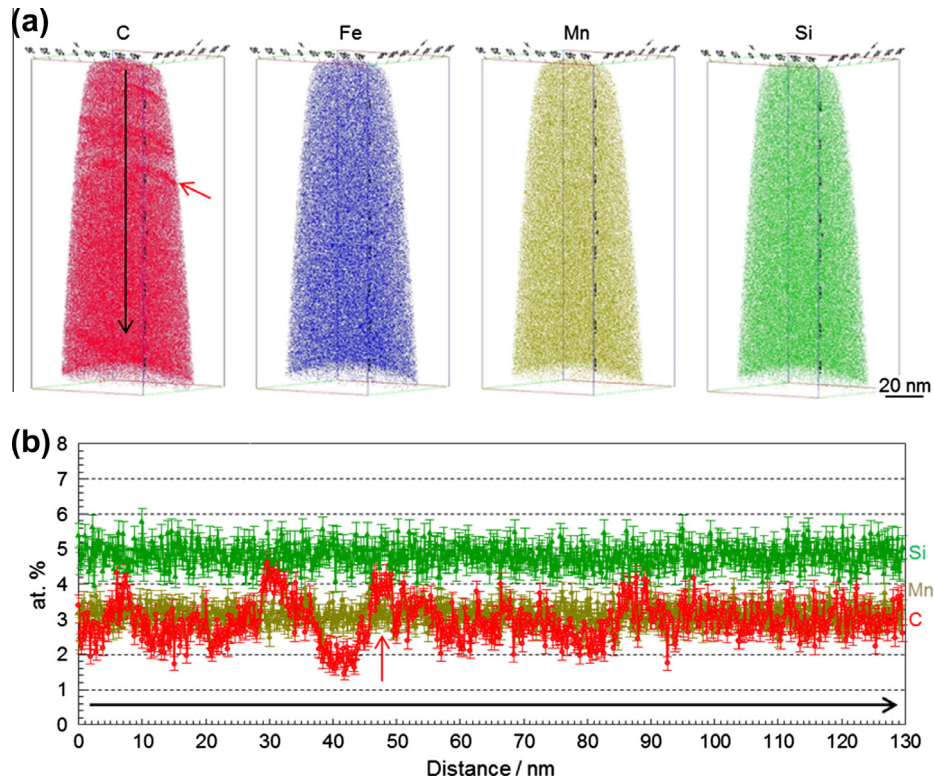


Fig. 7. (a) Three-dimensional (3-D) atom maps of C, Fe, Mn and Si of the as-quenched specimen, and (b) C, Mn, Si concentration profiles along the black arrow indicated in the C atom map in (a). Red arrows in the C atom map (a) and the C concentration profile (b) indicate the same position. The error bars in (b) represent the one-sigma statistical error. (For interpretation of the references to color in this figure legend, the reader is referred to the web version of this article.)

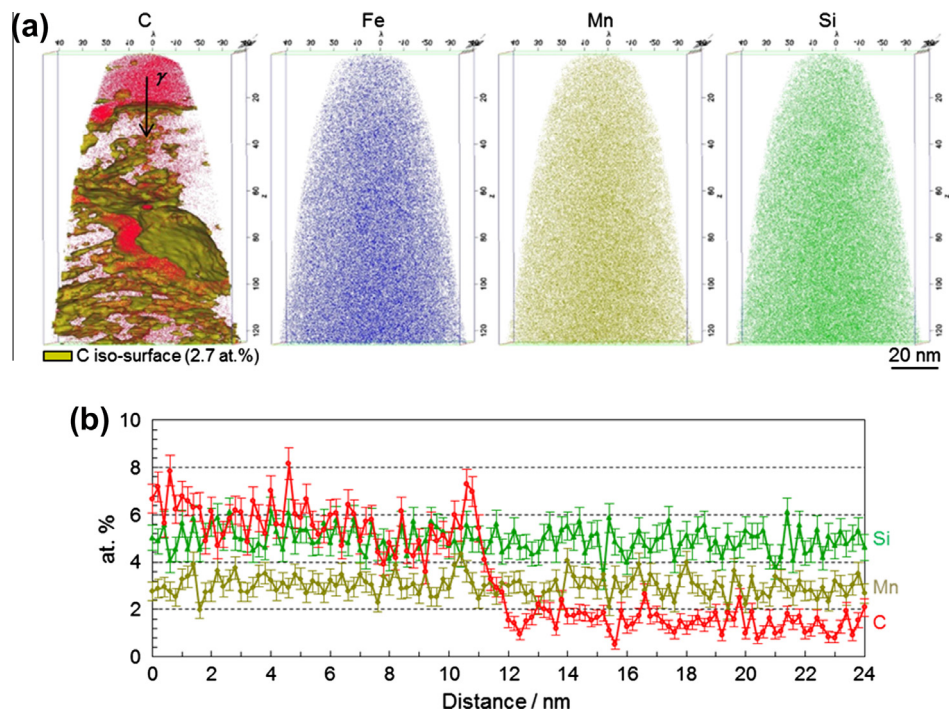


Fig. 8. (a) 3-D atom maps of C, Fe, Mn and Si of the specimen tempered at 400 °C for 10 s, (b) C, Mn, Si concentration profiles along the arrow indicated in the C atom map in (a). The yellow surfaces in (a) are the isoconcentration surfaces with 2.7 at.% C. The error bars in (b) represent the one-sigma statistical error.  $\gamma$ : austenite. (For interpretation of the references to colour in this figure legend, the reader is referred to the web version of this article.)

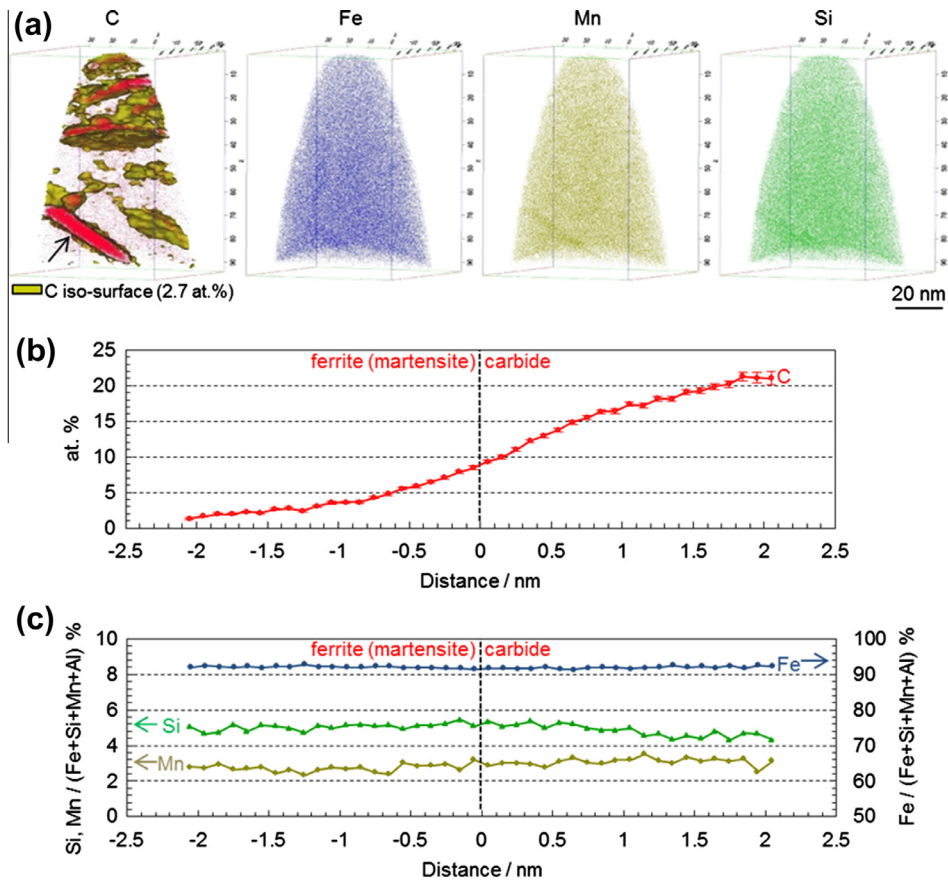


Fig. 9. (a) 3-D atom maps of C, Fe, Mn and Si of the specimen tempered at 400 °C for 300 s, (b) average compositions of C relative to the position of the 10 at.% C isosurface around the carbide indicated by the arrow in (a), (c) average substitutional atomic fraction of Fe, Mn, Si relative to the position of the 10 at.% C isosurface around the carbide indicated by the arrow in (a). The yellow surfaces in (a) are the isoconcentration surfaces with 2.7 at.% C. The error bars in (b) represent the one-sigma statistical error. (For interpretation of the references to color in this figure legend, the reader is referred to the web version of this article.)

atom map (Fig. 10a). C, Mn, Si proxigrams across the 5 at.% carbon isoconcentration surface created inside the cylinder are plotted in Fig. 10c. The shape and size of the carbon-enriched region are obviously different from the carbides shown in Fig. 9. The carbon concentration inside the enriched region is 6–10 at.%, which is similar to that in the austenite shown in Fig. 6. From the size and carbon concentration, this region is hence identified as austenite. Pileup of carbon around the interface in the austenite region is also found, which is attributed to the slow carbon diffusion in austenite. Interestingly, Mn also partitions between martensite and austenite in this region.

The change in carbon concentration in austenite during tempering at 400 °C analyzed by APT is shown in Fig. 11. The carbon concentration in the austenite in the as-quenched specimen is identical to the bulk composition because no carbon partitioning to austenite during water-quenching was detected as mentioned above. The austenite carbon concentrations in the tempered specimens shown in Fig. 11 are the analyzed values in the austenite regions at least 2 nm away from the interface between martensite and austenite in order to exclude the influence of the artifact around the interface (i.e. the local magnification effect

which may broaden the interface). The interface was in all cases defined to be the median of the carbon concentration gradient between two phases. The austenite carbon concentration rapidly increased with tempering for 10 s and then gradually increased upon further tempering. These results quantitatively reveal carbon partitioning from martensite into austenite in the absence of influences by bainite transformation.

#### 4. Discussion

##### 4.1. Comparison between carbon concentrations in austenite as measured via XRD and APT

Here we compare the carbon concentrations in austenite as measured by XRD (Fig. 2) and APT (Fig. 11), respectively. The changes in austenite carbon concentration during tempering as measured by XRD and APT showed a similar trend. In either case, the carbon concentration increased with tempering time. However, the carbon concentrations obtained by XRD were much lower than those obtained by APT. Several reasons may cause this difference. One is the difference in the probed regions. Clarke

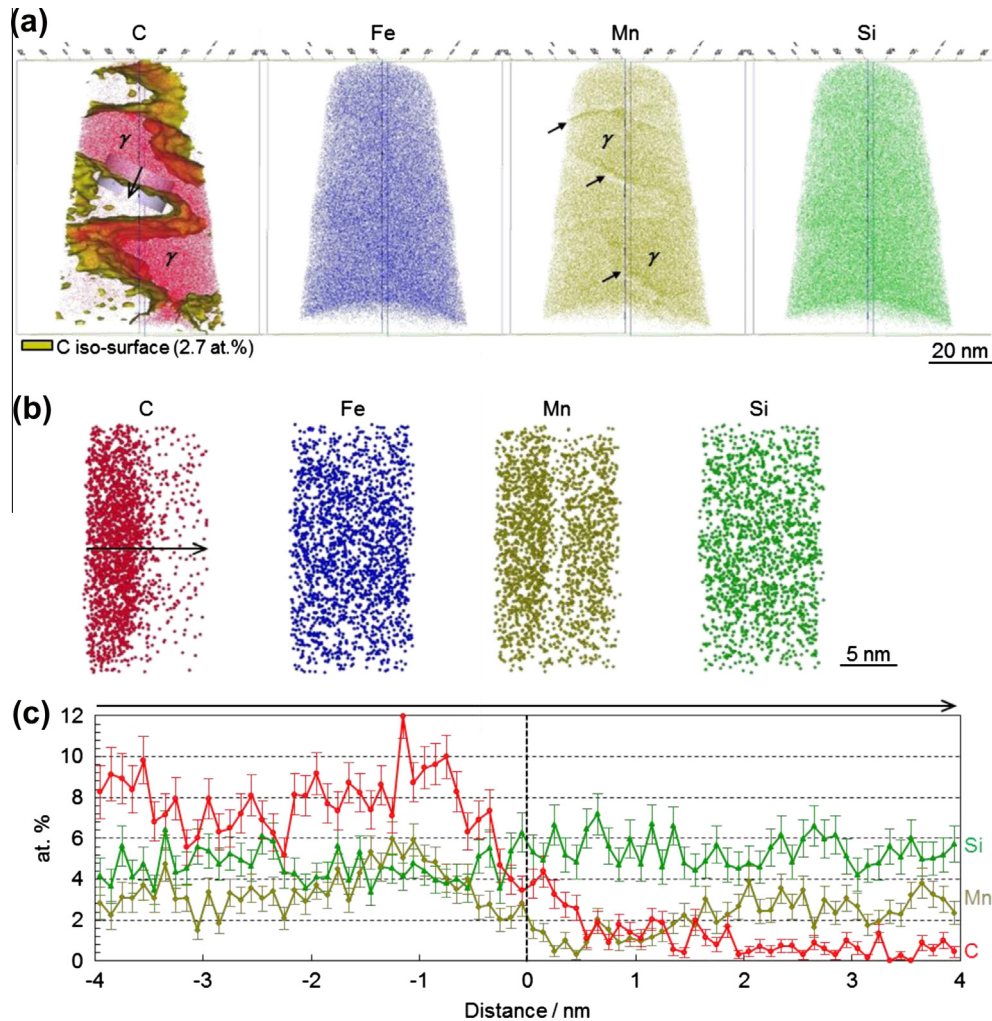


Fig. 10. (a) 3-D atom maps of C, Fe, Mn and Si of the specimen tempered at 400 °C for 300 s, (b) atom maps of C, Fe, Mn and Si inside the cylinder in (a), (c) average compositions of C, Si, Mn relative to the position of the 5 at.% C isosurface inside the cylinder in (a). The yellow surfaces in (a) are the isoconcentration surfaces with 2.7 at.% C. The error bars in (c) represent the one-sigma statistical error. The arrows in Mn atom map in (a) show Mn partitioning from martensite to austenite.  $\gamma$ : austenite. (For interpretation of the references to colour in this figure legend, the reader is referred to the web version of this article.)

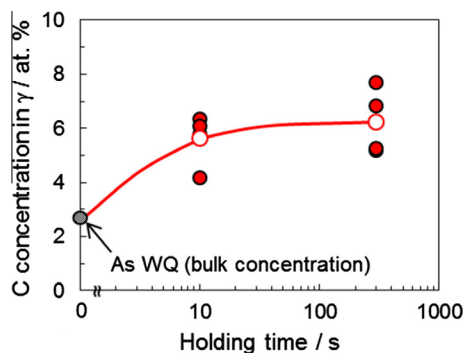


Fig. 11. Change in C concentration in  $\gamma$  during partitioning at 400 °C. Solid symbols show the individual C concentrations obtained from the APT results. Open symbols show the average C concentration of the measured values at each partitioning time.  $\gamma$ : austenite, WQ: water-quenching.

et al. [51] observed that the austenite carbon concentrations measured by APT were less than those obtained by XRD.

They mentioned that the carbon-enriched regions observed in the APT data were regions which might have partially transformed to martensite during final cooling after the partitioning step. Indeed, as mentioned in Section 2.3, it is difficult to distinguish retained austenite at room temperature from martensite, which forms during final cooling due to insufficient carbon enrichment, by APT alone without correlative TEM observation such as applied in this study. On the other hand, the austenite carbon concentrations measured by XRD are those in the retained austenite that prevails after final cooling to room temperature, excluding the regions with relatively low carbon concentration that transform to martensite during final cooling. This difference in the probed regions may cause the discrepancy of carbon concentration data obtained by the two methods. However, the austenite in this study is already stable at room temperature in the as-quenched state, and its stability does not drop during tempering. This means that all austenite that is present at 400 °C prevails after cooling to

room temperature. Therefore, we expect that the austenite regions measured by XRD and APT, respectively, were the same in this study. It also must be noted that the carbon concentrations obtained by APT were higher than those obtained by XRD in the present study. This is the opposite trend as compared to the results reported in Ref. [51].

An alternative reason is the carbon inhomogeneity inside the austenite. The carbon concentration obtained by APT provides local information, whereas that obtained by XRD is statistical information. The APT results shown in Fig. 11 reveal some scatter at each tempering time. This scatter may be caused by the size of the austenite (i.e. carbon diffusion length), which has been reported in studies on bainite [40,52]. However, it is not clear whether this effect really applies to the case of the current Q&P heat treatment and further quantitative investigation is needed. Even taking into account the scatter in the APT data, the carbon concentration obtained by XRD is still lower than the lowest value obtained by APT.

Another possible reason for the difference is the compressive stress caused by the martensite transformation. The austenite carbon concentration of the as-quenched specimen was calculated to be below zero from the lattice parameter measured by XRD. This might be due to the fact that the retained austenite in the as-quenched specimen was compressed due to martensite transformation of its surrounding region such as reported in Ref. [53]. The increase in the austenite lattice parameter by tempering is, therefore, considered to be caused not only by the carbon enrichment into austenite but also by the release of the compressive stress. In addition, it is not clear whether the compressive stress is completely released under each tempering condition or not. Therefore, the carbon concentrations obtained by XRD are not quantitatively reliable in this case. The results obtained by APT in this study are considered to support the results obtained via in situ neutron measurement reported by Bigg et al. [22] from the atomic-scale quantitative point of view.

#### 4.2. C distribution in the as-quenched specimen

We observed no carbon partitioning from martensite to austenite in the as-quenched specimen (Fig. 7). On the other hand, carbon partitioning to film-like austenite in as-quenched martensite has been reported in low carbon steels [45–47]. This difference is attributed to the fact that the carbon diffusion length in austenite after the martensite transformation was very small in the present study because the  $M_s$  temperature of the current alloy (205 °C) is much lower than that of low carbon steels (typically above 400 °C). Even if the steel is held at 200 °C (just below its  $M_s$  temperature) for 1 s, the carbon diffusion length in austenite is 0.03 nm (according to the diffusion coefficient reported in Ref. [54]), which is much smaller than for the case that the steel is held at 400 °C for 1 s where the carbon diffusion length in austenite is 9.6 nm. Furthermore, the carbon diffusion length in austenite during sample storage

at 25 °C (room temperature) for 365 days is 0.001 nm. Therefore, no carbon enrichment in austenite must occur in the as-quenched specimen in the present study unlike the case observed in the previous studies that were conducted using low carbon steels with a higher  $M_s$  temperature. On the other hand, the carbon diffusion length in ferrite at 200 °C for 1 s is 52 nm (according to the diffusion coefficient reported in Ref. [55]). Hence it is possible for carbon to segregate to dislocations and interfaces in martensite, or even to martensite–austenite interfaces, which was indeed detected in the form of carbon fluctuation in Fig. 7. The fluctuation in carbon concentration is, however, smaller in the region below the position that is marked by the red arrows in Fig. 7a and b. This region might be austenite where only negligible carbon diffusion occurs. Corresponding phase identification using the APT/TEM correlative method mentioned in Section 3.3 was, however, not applicable to the as-quenched specimen since the retained austenite in the as-quenched specimen was very unstable. The austenite is stabilized mainly by hydrostatic stress caused by the martensite transformation of its surrounding region [53,56], hence it readily transforms into martensite when exposed to the surface upon APT/TEM preparation where the stress is released. Furthermore, even in the tempered specimen in which austenite was much more stable due to its higher carbon concentration owing to carbon partitioning from martensite, we observed that some portion of austenite transformed into martensite due to FIB damage caused during APT sample preparation. Because of these two reasons, no austenite was identified in the APT samples during TEM inspection.

#### 4.3. Comparison between experimental results and constrained carbon equilibrium (CCE) theory

In this section, the experimentally observed carbon partitioning behavior is compared to the CCE theory proposed by Speer et al. [11]. The CCE theory predicts the carbon concentration in austenite under the condition that (1) the chemical potential of carbon is identical in ferrite (or martensite) and austenite and (2) the atomic balancing proceeds under the assumption that the interface between ferrite and austenite does not migrate. These conditions are represented by the following equations [11]:

$$\mu_{CCE}^{\gamma} = \mu_{CCE}^{\alpha} \quad (2)$$

$$f_{CCE}^{\gamma}(1 - X_{CCE}^{\gamma}) = f_i^{\gamma}(1 - X_C^{alloy}) \quad (3)$$

$$f_{CCE}^{\alpha} X_{CCE}^{\alpha} + f_{CCE}^{\gamma} X_{CCE}^{\gamma} = X_C^{alloy} \quad (4)$$

$$f_{CCE}^{\alpha} + f_{CCE}^{\gamma} = 1 \quad (5)$$

where  $\mu_{CCE}^{\gamma}$  and  $\mu_{CCE}^{\alpha}$  are the chemical potentials of carbon in austenite and ferrite, respectively.  $f_i^{\gamma}$ ,  $f_{CCE}^{\gamma}$  and  $f_{CCE}^{\alpha}$  represent the initial austenite mole fraction before the partitioning step and the austenite and ferrite mole fractions under CCE conditions, respectively.  $X_C^{alloy}$ ,  $X_{CCE}^{\gamma}$  and  $X_{CCE}^{\alpha}$  represent the alloy carbon concentration,

and the carbon concentration in austenite and ferrite under CCE condition, respectively. The carbon concentration is expressed in terms of atomic (or mole) fraction. Eq. (3) expresses the mass balance of the substitutional elements. Eq. (4) expresses the mass balance of carbon. Eq. (5) describes the relationship between the phase fractions. Regarding condition (1), Speer et al. [11] used a simplified relationship [57] between the carbon activities in ferrite and austenite for the Fe–C binary system, as a simple model case. However, the chemical potential of carbon in each phase is influenced by the other alloying elements such as Si and Mn. In most previous works, the carbon concentration in austenite under CCE conditions is approximated assuming that virtually all of the carbon partitions to austenite. This approximation is appropriate for low carbon steels with high austenite volume fraction at the quench temperature. However, the difference between approximated values (assuming that all carbon partitions to austenite) and strictly calculated values becomes larger with a lower austenite volume fraction and/or higher carbon concentration [11], as the case in this study. In order to take account of the influence of the other elements in a rigorous calculation, we apply a similar method as suggested by Tsuchiyama et al. [58]. At first, free energy curves for ferrite and austenite at 400 °C were calculated by Thermo-Calc using the data base TCFE6 (Fig. 12). These curves were then fitted by quadratic functions. The carbon concentrations in each phase, at which the tangents to the ferrite and austenite free energy curves intersect the carbon axis (i.e.  $x(c) = 1$ ,  $x(c)$  represents atomic fraction of carbon) at a single point

(Fig. 12a), were calculated under the condition (2) described above. The accuracy of this method was confirmed by comparing the values in the case that Speer et al. demonstrated in Ref. [11] (Fe–0.5 wt.% C,  $f_i^\gamma = 25\%$ ). The austenite carbon concentration in their calculation was 1.97 wt.%, whereas the calculated austenite carbon concentration obtained by the method used in this study was 1.966 wt.%, i.e. both values are very close.

The calculated austenite carbon concentration in the present case is 19.9 at.% (5.05 wt.%) shown as  $X_{CCE}^\gamma$  in Fig. 12b. The experimentally analyzed austenite carbon concentration range at 300 s tempering state, which seems to be almost saturated (Fig. 11), is also shown in Fig. 12b as  $X_{Cexp}^\gamma$ . The experimental value is much lower than the calculated austenite carbon concentration under the CCE condition. The main reason for this discrepancy is considered to be the carbide precipitation inside the martensite during tempering as shown in Figs. 4 and 9, regardless of the high Si content. Kozeschnik and Bhadeshia [59] reported that Si strongly suppresses carbide precipitation in austenite, but is less effective in ferrite (or martensite) because the driving force for the precipitation is too high due to the low solubility of carbon in ferrite. Especially in the case of the present steel in which the carbon content is high, carbide precipitation in martensite is considered to be practically unavoidable. Moreover, if the carbide observed in this study is a transition carbide such as  $\epsilon$ -carbide, Si does not have significant effect to suppress the precipitation of this transition carbide [12,49]. As Speer et al. [12] pointed out, it is important to choose appropriate chemical compositions in order to avoid

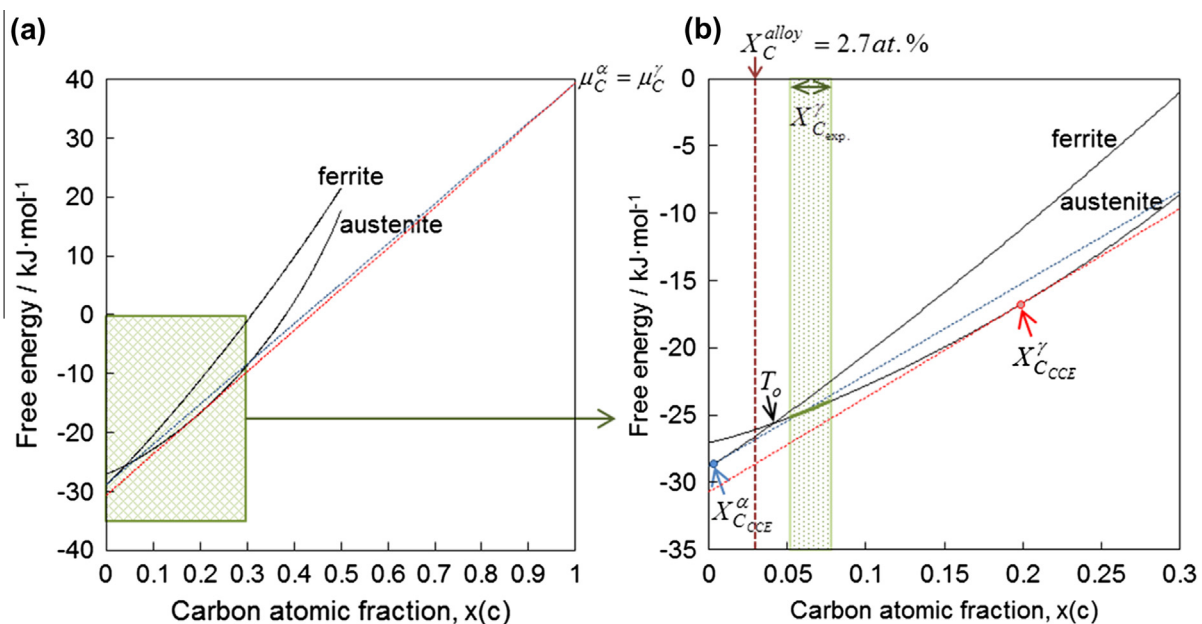


Fig. 12. Comparison between carbon atomic fraction in  $\gamma$  at 400 °C calculated under the constrained carbon equilibrium (CCE) condition and that experimentally obtained by APT. (b) Magnified figure inside the green square in (a).  $\mu_{CCE}^\alpha$  and  $\mu_{CCE}^\gamma$  are the carbon chemical potentials in austenite and ferrite, respectively.  $X_C^{alloy}$ ,  $X_{CCE}^\gamma$ ,  $X_{CCE}^\alpha$  and  $X_{Cexp}^\gamma$  represent the alloy carbon concentration, carbon concentration in austenite and ferrite under CCE condition and experimentally obtained carbon concentration, respectively.  $T_0$  represents the carbon concentration where free energies in ferrite and austenite are identical.

carbide precipitation for the ideal Q&P condition. In addition, predictions that include carbide precipitation in martensite are also needed in order to achieve a more precise estimate of the carbon concentration in austenite after Q&P heat treatments. This is relevant since some carbide precipitation in martensite seems to be unavoidable, even in low carbon steels [18].

It also should be noted that the experimentally analyzed carbon concentration in austenite is higher than the carbon concentration at the point  $T_0$  where the free energies in ferrite and austenite are identical. For the case of the displacive mechanism, bainite transformation is considered to stop when austenite carbon concentration reaches  $T_0$  (or  $T'_0 (<T_0)$ , when accounting for the stored energy of bainite) [60], because there is no driving force for the transformation from fcc to bcc without carbon diffusion if the austenite carbon concentration is above  $T_0$ . The results demonstrate that carbon can enrich in austenite beyond the  $T_0$  concentration via carbon partitioning from martensite to austenite without the occurrence of phase transformations (be it displacive or reconstructive) in the Q&P heat treatment, as predicted by Speer et al. [11].

#### 4.4. Mn partitioning between martensite and austenite

Mn partitioning from martensite into austenite was also observed in the specimen tempered at 400 °C for 300 s (Fig. 10). There seems to be few previous studies mentioning Mn partitioning from martensite to austenite during tempering of martensitic steels containing austenite at such a low temperature and short tempering time. However, Mn partitioning has indeed been observed during tempering of a low carbon maraging TRIP steel at 450 °C for much longer tempering time (48 h) [61,62]. In addition, Santofimia et al. [63] recently reported Mn partitioning at a similar partitioning condition (400 °C for 50 s) as the current study. On the other hand, such partitioning of Mn was not observed in the current specimen tempered for 10 s (Fig. 8). This means that Mn should have partitioned after the partitioning of carbon due to the slower diffusion coefficient of Mn. The Mn partitioning may also indicate interface migration as recently proposed [14–16,19,20]. However, even if the interface migrates together with the Mn partitioning, the interface motion should have a negligible influence on the carbon partitioning to austenite, especially at the early stage of the tempering, because carbon partitioning already occurs after 10 s tempering at 400 °C without Mn partitioning (Fig. 8). In addition, the Mn diffusion range was below 2 nm across the interface at 300 s tempering, which is very small compared to the size of austenite grains (Figs. 4 and 5). Even though Mn partitioning has thus only a small effect on carbon partitioning, it is yet important to register as it might affect the mechanical properties after longer tempering times, when Mn partitioning becomes more pronounced.

## 5. Conclusions

Carbon partitioning from martensite to austenite during the partitioning step in a Q&P heat treatment was quantitatively investigated at the atomic scale by APT and correlative TEM observations. A model steel with  $M_f$  temperature below room temperature was designed in order to separate the carbon partitioning between martensite and austenite from the bainite transformation. Approximately 8 vol.% of austenite existed in the as-quenched specimen. We showed by XRD and dilatometry that austenite decomposition via bainite transformation did not occur during tempering at 400 °C. No carbon enrichment in austenite was detected in the as-quenched specimen. In the tempered states, carbon enrichment in austenite was observed with a carbon concentration inside the austenite of 5–8 at.%. The results quantitatively reveal carbon partitioning from martensite into austenite excluding any interfering effects from the bainite transformation during the Q&P heat treatment. The results are essential for better understanding of microstructural changes, including the bainite transformation and carbide precipitation in martensite during Q&P heat treatments with the aim of achieving advanced alloy design that is rooted in an atomistic understanding of the underlying partitioning phenomena.

## References

- [1] Matsuoka S, Hasegawa K, Tanaka Y. JFE Tech Rep 2007;10:13.
- [2] Hasegawa K, Kaneko S, Seto K. JFE Tech Rep 2013;18:80.
- [3] Sakuma Y, Matsumura O, Akisue O. ISIJ Int 1991;31:1348.
- [4] De Cooman BC, Speer JG. Steel Res Int 2006;77:634.
- [5] Matlock DK, Speer JG. In: Lee HC, editor. Proc 3rd int conf on advanced structural steels. Gyeongju: Korean Institute of Metals and Materials; 2006. p. 774.
- [6] Raabe D, Ponge D, Dmitrieva O, Sander B. Adv Eng Mater 2009;11:547.
- [7] Caballero FG, Bhadeshia HKDH, Mawella JA, Jones DG, Brown P. Mater Sci Technol 2001;17:517.
- [8] Caballero FG, Bhadeshia HKDH. Curr Opin Solid State Mater Sci 2004;8:251.
- [9] Ponge D, Millán J, Dmitrieva O, Sander B, Kostka A, Raabe D. In: Higashida K, Tsuji N, editors. Proc 2nd int symp steel sci (ISSS 2009). Kyoto: The Iron and Steel Institute of Japan; 2009. p. 121.
- [10] Raabe D, Ponge D, Dmitrieva O, Sander B. Scripta Mater 2009;60:1141.
- [11] Speer JG, Matlock DK, De Cooman BC, Schroth JG. Acta Mater 2003;51:2611.
- [12] Speer JG, Streicher AM, Matlock DK, Rizzo FC, Krauss G. In: Damm EB, Merwin M, editors. Austenite formation and decomposition. Warrendale, PA: TMS/ISS; 2003. p. 505.
- [13] Kim SJ, Kim HS, De Cooman BC. In: Proc mater sci technol. Detroit, MI: MS&T; 2007. p. 73.
- [14] Zhong N, Wang X, Rong Y, Wang L. J Mater Sci Technol 2006;22:751.
- [15] Santofimia MJ, Nguyen-Minh T, Zhao L, Petrov R, Sabirov I, Sietsma J. Mater Sci Eng A 2010;527:6429.
- [16] Santofimia MJ, Zhao L, Petrov R, Kwakernaak C, Sloof WG, Sietsma J. Acta Mater 2011;59:6059.
- [17] Seto K, Matsuda H. Mater Sci Technol 2013;29:1158.
- [18] Santofimia MJ, Zhao L, Sietsma J. Metall Mater Trans A 2009;40A:46.

- [19] Speer JG, Hackenberg RE, De Cooman BC, Matlock DK. *Philos Mag Lett* 2007;87:379.
- [20] Santofimia MJ, Speer JG, Clarke AJ, Zhao L, Sietsma J. *Acta Mater* 2009;57:4548.
- [21] Bhadeshia HKDH, Edmonds DV. *Metall Trans A* 1979;10A:895.
- [22] Bigg TD, Matlock DK, Speer JG, Edmonds DV. *Solid State Phenom* 2011;172–174:827.
- [23] Cerezo A, Godfrey TJ, Smith GDW. *Rev Sci Instrum* 1988;59:862.
- [24] Blavette D, Deconihout B, Bostel A, Sarrau JM, Bouet M, Menand A. *Rev Sci Instrum* 1993;64:2911.
- [25] Miller MK, Cerezo A, Hetherington MG, Smith GDW. *Atom probe field ion microscopy*. Oxford: Oxford University Press; 1996.
- [26] Hono K. *Acta Mater* 1999;47:3127.
- [27] Miller MK. *Atom probe tomography analysis at the atomic scale*. New York: Kluwer Academic/Plenum; 2000.
- [28] Kelly TF, Miller MK. *Rev Sci Instrum* 2007;78:031101.
- [29] Seidman D. *Annu Rev Mater Sci* 2007;37:127.
- [30] Choi P, da Silva M, Klement U, Al-Kassab T, Kirchheim R. *Acta Mater* 2005;53:4473.
- [31] Marquis EA, Choi P, Danoix F, Kruska K, Lozano-Perez S, Ponge D, et al. *Microsc Today* 2012;20:44.
- [32] Duarte MJ, Klemm J, Klemm SO, Mayrhofer KJJ, Stratmann M, Borodin S, et al. *Science* 2013;341:372.
- [33] Koistinen DP, Marburger RE. *Acta Metall* 1959;7:59.
- [34] McDermid JR, Zurob HS, Bian Y. *Metall Mater Trans A* 2011;42A:3627.
- [35] Ruhl R, Cohen M. *Trans TMS-AIME* 1969;245:241.
- [36] Dyson DJ, Holmes B. *J Iron Steel Inst* 1970;208:469.
- [37] Thompson K, Sebastian J, Gerstl S. *Ultramicroscopy* 2007;107:124.
- [38] Li YJ, Choi P, Borchers C, Westerkamp S, Goto S, Raabe D, et al. *Acta Mater* 2011;59:3965.
- [39] Li YJ, Choi P, Goto S, Borchers C, Raabe D, Kirchheim R. *Acta Mater* 2012;60:4005.
- [40] Seol J, Raabe D, Choi P, Im Y, Park C. *Acta Mater* 2012;60:6183.
- [41] Moeck P, Rouvimov S, Rauch EF, Véron M, Kirmse H, Häusler I, et al. *Cryst Res Technol* 2011;46:589.
- [42] Rauch EF, Portillo J, Nicolopoulos S, Bultreys D, Rouvimov S, Moeck P. *Z Kristallogr* 2010;225:103.
- [43] Herbig M, Raabe D, Li YJ, Choi P, Zaefferer S, Goto S. *Physical Review Letters*, submitted for publication.
- [44] Cheng L, Brakman CM, Korevaar BM, Mittemeijer EJ. *Metall Trans A* 1988;19A:2415.
- [45] Sarikaya M, Thomas G, Steeds JW, Barnard SJ, Smith GDW. In: Aaronson HI, editor. *Proc int conf on solid to solid phase transformations*. Warrendale, PA: The Metallurgical Society; 1982. p. 1421.
- [46] Sherman DH, Cross SM, Kim S, Grandjean F, Long GJ, Miller MK. *Metall Mater Trans A* 2007;38A:1698.
- [47] Morito S, Oh-ishi K, Hono K, Ohba T. *ISIJ Int* 2011;51:1200.
- [48] Hellman OC, Vandenbroucke JA, Rusing J, Isheim D, Seidman DN. *Microsc Microanal* 2000;6:437.
- [49] Miyamoto G, Oh JC, Hono K, Furuhashi T, Maki T. *Acta Mater* 2007;55:5027.
- [50] Miller MK, Hetherington MG. *Surf Sci* 1991;246:442.
- [51] Clarke AJ, Speer JG, Miller MK, Hackenberg RE, Edmonds DV, Matlock DK, et al. *Acta Mater* 2008;56:16.
- [52] Caballero FG, Miller MK, Clarke AJ, Garcia-Mateo C. *Scripta Mater* 2010;63:442.
- [53] Golovchiner KY. *Fiz Metal Metalloved* 1974;37:126.
- [54] Smith RP. *Trans TMS-AIME* 1964;230:476.
- [55] Taylor KA, Cohen M. *Progr Mater Sci* 1992;36:225.
- [56] Patel JR, Cohen M. *Acta Metall* 1953;1:531.
- [57] Bhadeshia HKDH. *Met Sci* 1981;15:175.
- [58] Tsuchiyama T, Tobata J, Tao T, Nakada N, Takaki S. *Mater Sci Eng A* 2012;532:585.
- [59] Kozeschnik E, Bhadeshia HKDH. *Mater Sci Technol* 2008;24:343.
- [60] Bhadeshia HKDH. *Acta Metall* 1981;29:1117.
- [61] Dmitrieva O, Ponge D, Inden G, Millán J, Choi P, Sietsma J, et al. *Acta Mater* 2011;59:364.
- [62] Raabe D, Sandlöbes S, Millán J, Ponge D, Assadi H, Herbig M, et al. *Acta Mater* 2013;61:6132.
- [63] Santofimia MJ, Zhao L, Povstugar I, Choi P, Raabe D, Sietsma J. In: Furuhashi T, Numakura H, Ushioda K, editors. *Proc 3rd int symp steel sci (ISSS 2012)*. Kyoto: The Iron and Steel Institute of Japan; 2012. p. 155.